SOLUS | SMART OPTICAL AND ULTRASOUND DIAGNOSTICS OF BREAST CANCER

Project title: Smart Optical and Ultrasound Diagnostics of Breast Cancer

Grant Agreement: 731877

Call identifier: H2020-ICT-2016-1

Topic: ICT-29-2016 Photonics KET 2016

Deliverable 4.6: Performance assessment of the single optode

Leader partner: Beneficiary 1, POLIMI

Author(s): Laura Di Sieno (POLIMI), Alessandro Ruggeri (MPD), Simone Tisa (MPD), Alberto Tosi (POLIMI), Alexander Flocke (iCHaus), Antonio Pifferi (POLIMI), Paola Taroni (POLIMI), Alberto Dalla Mora (POLIMI)

Work Package: 4

Estimated delivery: Month 36

Actual delivery: 31 October 2019

Type: Report

Dissemination level: Public

Table of contents

1. Introduction 2
2. Basic performance assessment (BIP protocol) 2
3. Capability to detect a localized inclusion (nEUROPt protocol) 8
4. Capability to retrieve optical properties (MEDPHOT protocol) 14
5. Conclusions 18
6. References 19

Abbreviations

BIP	Basic Instrument Performance
DR	Dynamic Range
DTOF	Distribution of Time-of-Flight
FWHM	Full-Width at Half-Maximum
IRF	Instrument Response Function
KPI	Key Performance Indicator
LD	Laser Diode
SDD	Source-Detector Distance
TDC	Time-to-Digital Converter

1. Introduction

The aim of this deliverable is the validation in laboratory settings of the first complete and fully-operative prototype of the single optode, which is the innovative building block of the SOLUS probe. This optode is capable to perform time domain diffuse optical measurements at different wavelengths with wide dynamic range, thus providing in a non-invasive way information about the composition of the tissue under investigation. The arrangement of 8 optodes around an ultrasound transducer (see Figure 1) will then allow to have diffuse optical tomography reconstructions of breast lesions guided by ultrasound imaging. More details about the single optode can be found in deliverable D1.4 (Complete smart optode). Its main components are the 8 integrated pulsed laser diodes and a large area time-gated single-photon detector with embedded time-to-digital converter. While the stand-alone components of the optode have been characterized in deliverable D4.5 (Performances assessment of optode components), this document carries out a comprehensive characterization of the single optode overall performances to verify its suitability for diffuse optical measurements. To this extent, well established protocols for diffuse optical instruments, such as BIP, nEUROPt and MEDPHOT, were adopted [1]-[3]. The optode is mounted into a mechanical holder able to host 4 complete optodes (see Figure 1). Here we report the characterization of optode number 4 as a stand-alone object embedding sources and detectors. In order to test the optode performances not only at few millimetres source-detector separations, sources of optode number 2 have also been used in combination with detector of optode number 4, with a larger source-detector separation, a condition which is also met in the multimodal SOLUS system.

The report is organized as follows: Section 2 describes the optode basic hardware performances assessed following the BIP protocol; Section 3 deals with the capability of the optode to detect and localize absorption perturbations within scattering media, assessed following the nEUROPt protocol; Section 4 reports the performances of the optode in the retrieval of optical properties of a homogeneous medium following the MEDPHOT protocol and, finally, in Section 5 the conclusions are drawn.

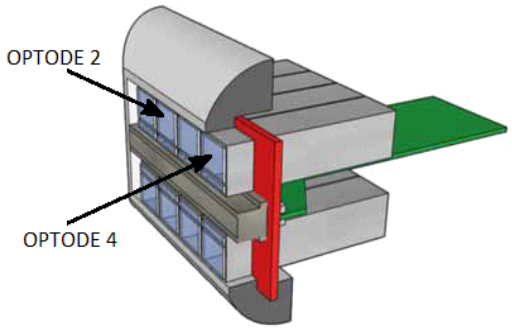

Figure 1. Sketch of the SOLUS probe showing the 2 assemblies of 4 optodes at opposite sides of the ultrasound transducer. The 2 optodes used for this report are highlighted.

2. Basic performance assessment (BIP protocol)

INTRODUCTION

The BIP protocol [1] deals with the assessment of the basic hardware performances of time domain instruments. It is composed of several tests whose aim is to assess the capability of the system to measure the distribution of time-of-flight (DTOF) and more specifically, its shape, signal-to-noise ratio and stability.

The protocol is composed of several tests which involve all the main parts of the system (source components - laser power, area and wavelength - and detection ones - responsivity and differential nonlinearity) as well as the system as a whole (shape and stability of the Instrument Response Function and afterpulsing ratio).

EXPERIMENTAL SETUP AND DATA ANALYSIS

Most of the measurements were made using the integrated laser at a repetition rate of 40 MHz. The DTOFs were recorded using the gated detector with a gate width of 8 ns and an active area which was tuned

depending on the desired count rate/signal level.

LASER OUTPUT POWER

For each laser die, the power was measured using a powermeter (S140C, Thorlabs GmbH, Germany). Due to the high divergence of the laser die, the light was focussed into the powermeter sensitive area using a 25 mm-diameter lens (numerical aperture 0.83, Edmund Optics, USA).

LASER EMISSION SPECTRUM

The emission spectrum of the eight laser dice was collected using a spectrometer (USB2000, Ocean Optics, USA). In order to take into account the spectral contribution given by all laser emission modes a thin layer of Teflon was put on the laser window. The light was then collected at few centimeters of distance using an optical fiber, which was connected to the spectrometer fiber input.

AREA

The area of the laser spot was estimated by drawing its contour on a graph paper (placed in contact with the optode surface) and then computing the area.

RESPONSIVITY

Due to the need of using a transmittance geometry (i.e. laser and detection chain placed on the opposite sides of a calibrated tissue phantom), the responsivity of the optode detection chain has been measured using an external laser driver, which drove 2 laser heads (one at 670 nm and one at 830 nm) and the detection chain (detector and timing electronics) of the optode. It is worth noting that, as specified in the BIP protocol, the responsivity measurement is not dependent on the laser characteristics, thus the measurement is not affected by the choice of an external laser source. The auxiliary output of the detector provided a pulse synchronous with the gate open, which was then given as a trigger input to the external laser driver.

Laser light exiting from the laser head was then coupled into a 600 µm-core fiber and, after an attenuation stage (i.e. optical u-bracket hosting a stack of variable optical attenuators), it entered in the 600 µm-core injection fiber. Photons re-emitted from the calibrated responsivity phantom were then collected by the optode detector that was put in contact with the phantom surface. The measurement was performed with one wavelength at a time. The power injected into the phantom (i.e. measured at the injection fiber tip) was measured using a powermeter (S140C, Thorlabs GmbH, Germany). Additionally, a dark acquisition (i.e. without laser light) was performed to allow the background subtraction in the post processing analysis.

The responsivity was computed with 1024 SPADs enabled (i.e. with an active area of around 5.1 mm^2) and, as defined by the BIP protocol, the overall acquisition time was 20 s (i.e. 1000 repetitions of 20 ms each). For the count rate, we had 500 kcps of signal (i.e. in addition to the dark count rate), thus possibly experiencing counting losses due to the dead-time of the time-to-digital converter (TDC). For that reason, the raw curves were processed to correct the counting loss, following the formula reported in Ref. [4].

DIFFERENTIAL NON LINEARITY

The calculation of the DNL was performed using a different procedure with respect to the one explained in the BIP procedure. Indeed, here we had two issues to be considered: i) the gating acquisition of the detector prevents the acquisition of the DNL of the whole time scale range with a single free running (i.e. non gated) acquisition; ii) the gate shape is not flat (even if just one SPAD is on), thus possibly mixing the effect of the DNL with the issues connected to the flatness of the gate. For those reasons, the DNL measurement was divided into several measurements corresponding to different delays of the SPAD gate (“gate delay” in the following) with respect to the TDC scale range. For each acquisition, the signal was integrated to reach a number of count of about 10^6 counts per channel to reduce the Poisson noise contribution below 1%. For each measurement at a given gate delay, only the flattest region of the gate

was used to compute the DNL correction coefficients (i.e. the multiplicative factors to get a flat distribution of photons in the different time bins of the histogram). The recovery of the DNL values for the whole scale was possible by moving the gate due to the non-standard acquisition of the DNL measurement. The deviation from the ideal case (i.e. same number of counts for all channels) was computed as the peak-to-peak difference normalized to the mean value of the DNL coefficient, similar to the definition provided in Ref. [1].

IRF SHAPE AND STABILITY

As predicted by the BIP protocol, the Instrument Response Function (IRF) shape and stability were also assessed using the lasers of optode 4. Due to the optode structure, it was not possible to acquire the IRF using the standard method (i.e. collection and detection fibers faced with a thin layer of diffuser in between). We measured the IRF placing the optode in contact with a black PVC plane with a groove connecting source and detector locations. A thin layer of diffusive ultrasound gel was spread on the PVC surface to prevent direct (not diffuse) light collection (see Ref. [5] for details). For the IRF stability, in a single measurement all laser diodes were tested when the initial stabilization phase (few minutes) was finished. LDs were continuously turned on after one another (from LD 1 to LD 8) and an acquisition of 20 ms was saved. The cycle of shining the 8 lasers was repeated till reaching 210 minutes of overall acquisition. To improve the signal-to-noise ratio, 50 repetitions were summed up, thus obtaining the 1 s acquisition time defined by the BIP protocol. Such a procedure allows us to decrease the contribution of Poisson noise without significantly affecting the results. The goal count-rate was set to around 500 kcps.
To assess the laser stability in terms of counts, the integral (with an actual acquisition time of 1 s) was computed on the raw curves. On the other hand, the DNL correction was applied before computing the FWHM and the temporal position of the curve (i.e. centroid), in order to avoid any distortion possibly impairing the results. The average value of the counts, FWHM and temporal position was computed on the last 30 minutes of acquisition.

AFTERPULSING RATIO

The afterpulsing ratio was computed as dictated by the BIP protocol. Indeed, 1000 acquisitions of 20 ms each were recorded and summed up, thus achieving the total 20 s acquisition time. As for the responsivity, the target count-rate was considered separate from the noise one, thus we targeted 1 Mcps above the background value. For that reason, as done for the responsivity, the curves were pre-processed to correct the counting loss effect.

Table 1. Values of power and spectrum (FWHM and central wavelength) computed for the 8 LDs of each optode.

LASER DIODE		**SPECTRUM**				**POWER**	
Number	Nominal wavelength (nm)	Central wavelength (nm)		FWHM (nm)		Average (mW)	
		Opt 4	Opt 2	Opt 4	Opt 2	Opt 4	Opt 2
LD 1	1064	1053	1054	24	23	4.8	4.7
LD 2	1030	1029	1029	18	18	3.7	3.4
LD 3	980	979	978	8	7	3.0	1.5
LD 4	940	938	937	15	14	4.0	4.8
LD 5	915	916	914	9	10	6.5	5.2
LD 6	830	838	837	11	12	1.3	1.3
LD 7	670	681	680	3	3	3.5	2.5
LD 8	635	646	646	3	3	1.1	1.8

RESULTS AND DISCUSSION

LASER OUTPUT POWER

The values of the average power provided by the laser of both optodes 2 and 4 are reported in Table 1. All the LDs have an average power larger than 1 mW (which is the original KPI 1 target) and most of them provided more than 3 mW. Additionally, it has been verified that there is a good uniformity among the two optodes (optode 4 and optode 2).

LASER EMISSION SPECTRUM

Table 1 reports also the figures of merit (central wavelength and FWHM) of the spectral shape of the lasers. In most cases the central wavelength is very close to the nominal value (with a maximum error of 10-11 nm). However, as expected, for longer wavelengths there is an increasingly larger spectral width (i.e. FWHM). This behavior can be noticed also in the graphs reported in Figure 2, showing the recorded spectra for the LDs of optode 4. The uniformity among the LDs of the two optodes is very good, as can be seen comparing the central wavelengths and FWHM reported in Table 1.

AREA

The laser spot size for all lasers was measured to be around 1500 x 500 μm (height x width) thus being the area about 0.75 mm^2.

RESPONSIVITY

The responsivity value obtained at 670 and 830 nm with an active area of 5.1 mm^2 are respectively $1.8 \cdot 10^{-6}$ and $5.1 \cdot 10^{-7}$ m^2sr. With respect to the value reported in deliverable D4.5 (for a detector with an active area of nearly 7 mm^2) here we achieved slightly higher results, which may be due to the improved optical coupling between the detector and the probe surface and to slightly different detector conditions (i.e. excess bias voltage, temperature, etc.).

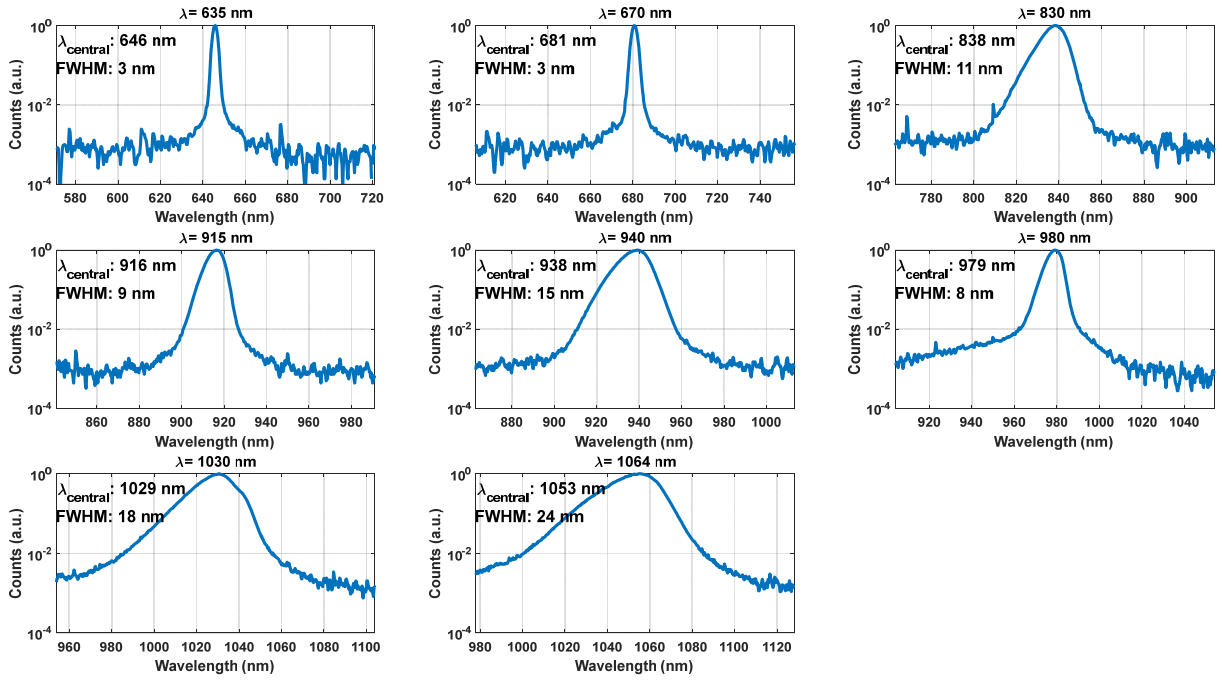

Figure 2. Spectral shape of the LDs for optode 4. Each graph (i.e. for each LD) reports the central wavelength and FWHM of the spectral shape (the values are reported in Table 1).

DIFFERENTIAL NON LINEARITY

As reported in Figure 3, the DNL coefficients range from 1.5 to -0.8 and the deviation from the ideal case (ε_{DNL}) is pretty large (70.7%). Notwithstanding the large value of the ε_{DNL} and the large bin-to-bin variability, using the computed coefficients, it is possible to efficiently correct the recorded DTOF, as shown in Figure 4.

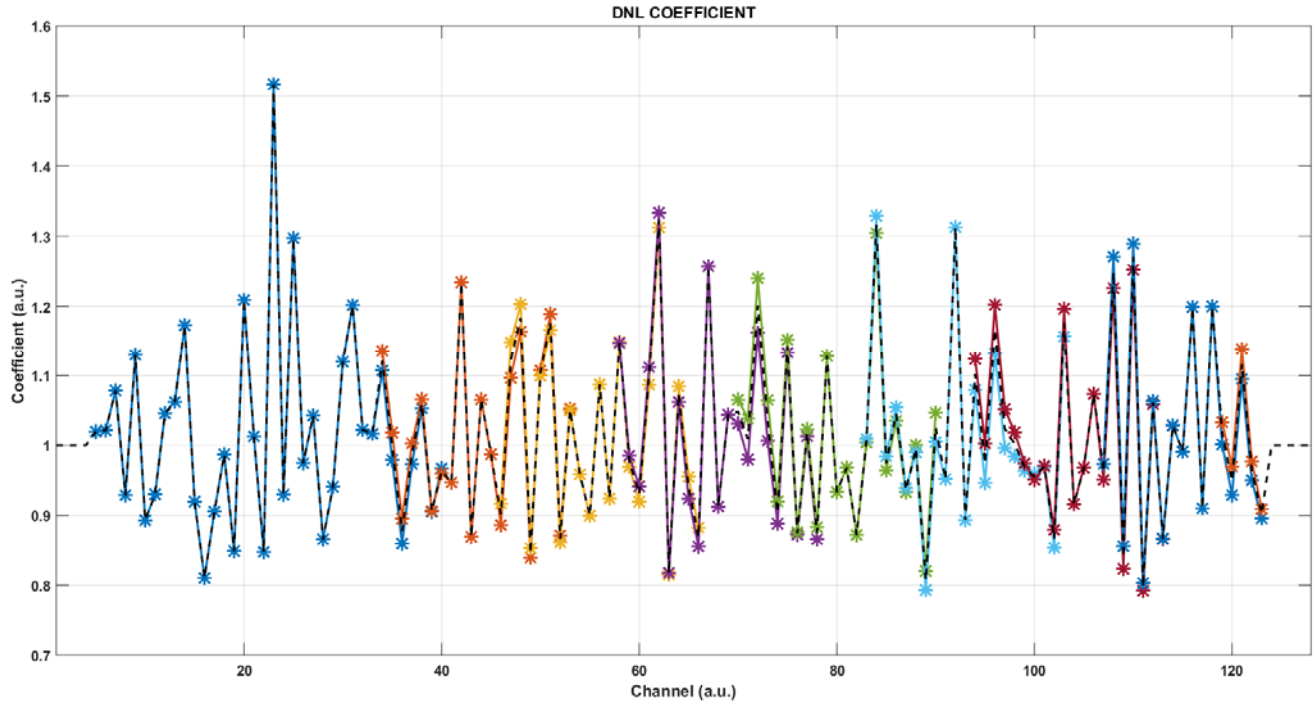

Figure 3. DNL coefficients computed from measurements (colors represent different acquisitions at different gate delays) and the average value of the DNL coefficients (black dashed line) used for measurements correction.

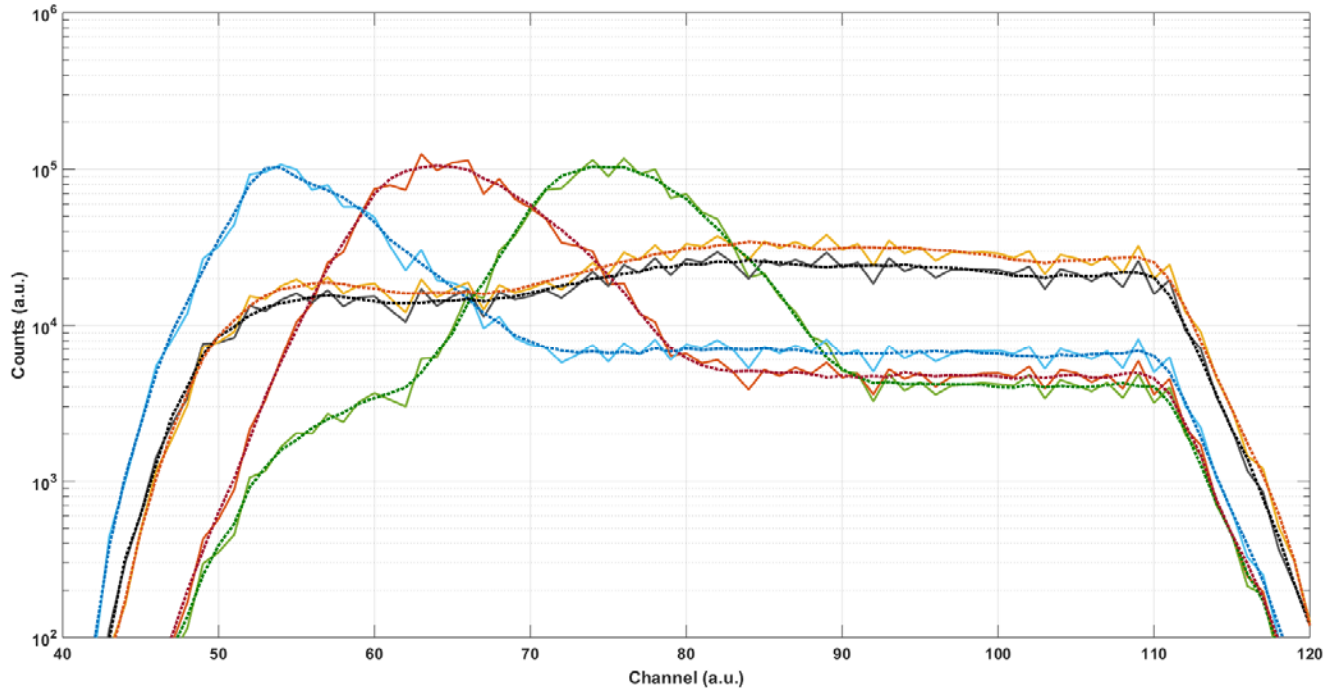

Figure 4. Curves recorded at different gate delays (different colors) before and after the DNL correction (respectively solid and dotted line).

IRF SHAPE AND STABILITY

Figure 5, Figure 6 and Figure 7 report respectively the stability in terms of counts, temporal position (i.e. centroid) and FWHM for each LD (single graph in the figure). The counts stability shows a decreasing trend over time, which exceeds the ±1% range. At any rate, it has to be noted that the trend is pretty slow

and monotonous. Indeed, in the worst case (i.e. LD 8, 635 nm) the number of counts varies of about ±1% over 30 minutes, thus being in line with state-of-the-art instruments.

On the other hand, both the temporal position and the FWHM are well stable during the 1 hour-acquisition: for all LDs, the oscillations around the mean value are inside the ±10 ps or ±1% range respectively. It is worth highlighting that here the FWHM of the IRFs acquired using different laser sources is, as expected, much larger than the FWHM of lasers pulses characterized in D4.5 (Performances assessment of optode components) due to the combination of different jitter contributions coming, for instance, from the finite detector response of few hundred ps and from the jitter of the TDC (see D4.5).

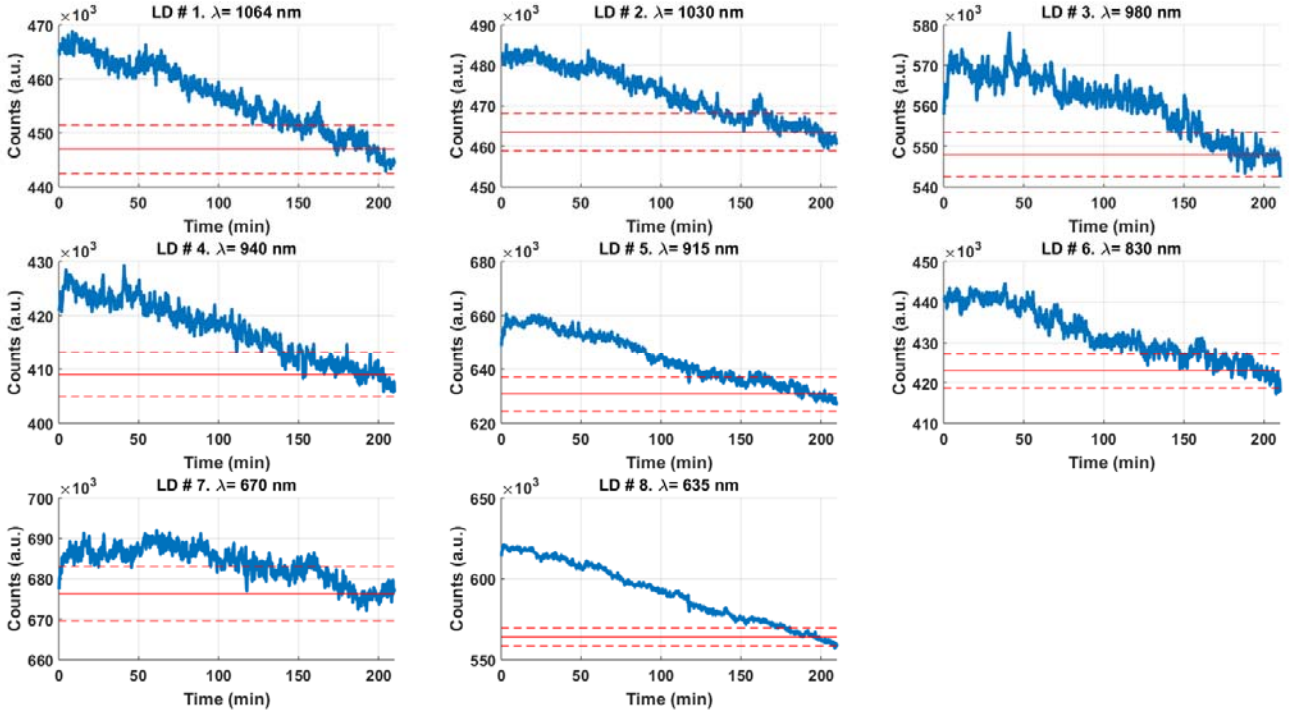

Figure 5. Stability of the number of counts acquired at each wavelength of optode 4. The red solid line is the mean value of counts (computed over the last 30 minutes of measurements), while red dotted lines correspond to the average ± 1%.

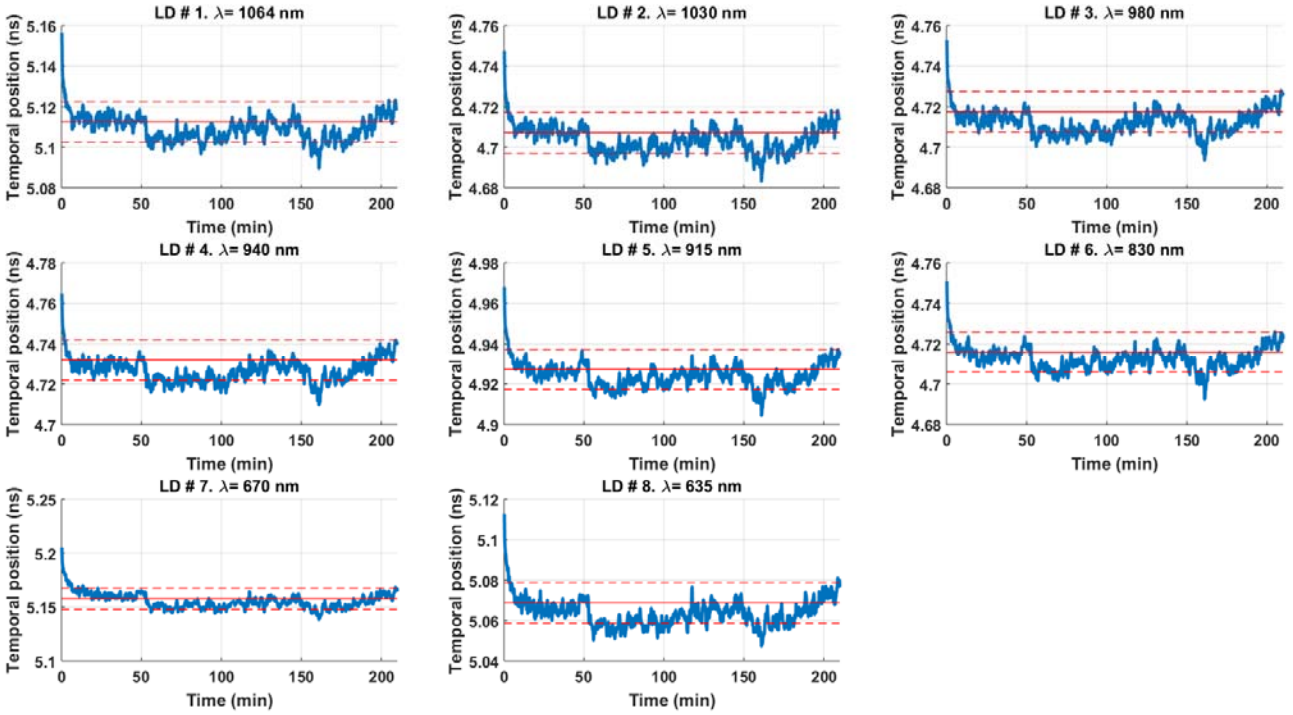

Figure 6. Stability of the temporal position (i.e. centroid) for each LD of optode 4. The red solid line is the mean value of temporal position (computed over the last 30 minutes of measurements), while red dotted lines correspond to the average ± 10 ps.

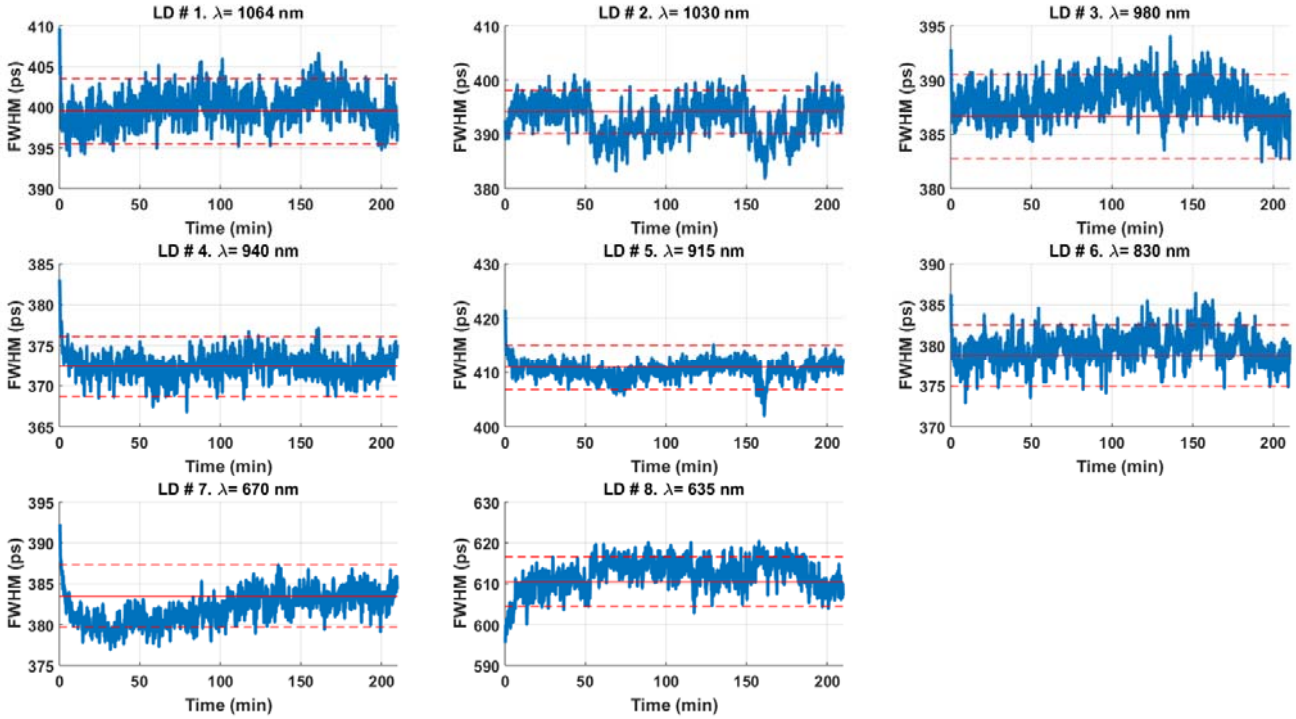

Figure 7. Stability of the FWHM for each LD of optode 4. The red solid line is the mean value of FWHM (computed over the last 30 minutes of measurements), while red dotted lines correspond to the average ± 1% ps.

AFTERPULSING RATIO

The computed afterpulsing ratio is about 5%, in line with the value reported in deliverable D4.5 (Performances assessment of optode components).

3. Capability to detect a localized inclusion (nEUROPt protocol)

INTRODUCTION

The nEUROPt protocol [2] is meant to assess through standardized tests the capability of diffuse optical instruments to detect, localize and quantify absorption changes within a homogeneous diffusive medium. In this deliverable, we will focus on the figures of merits defined by the nEUROPt protocol (i.e. contrast and contrast-to-noise ratio) and we will use them to assess the capability of the optode to detect a perturbation buried in depth (the so called “depth sensitivity”).

EXPERIMENTAL SETUP AND DATA ANALYSIS

To assess the depth sensitivity, we performed measurements where the perturbation was moved in depth with respect to the optode position. To perform this test, we made use of a calibrated liquid phantom made of a water mixture of Intralipid (to give scattering properties) and India ink (which act as absorber) in calibrated quantities [6] so as to have an absorption coefficient (μ_a) of 0.1 cm^{-1} and a reduced scattering coefficient (μ_s') of 10 cm^{-1} at 690 nm. The value of the optical properties of the phantom for all laser wavelengths are summarized in Table 2. The inclusion, as predicted by the nEUROPt protocol, is a totally absorbing one [7]-[8] (i.e. a black PVC cylinder) with 100 mm^3 volume and it features an absorbing perturbation ($\Delta\mu_a$) of 0.17 cm^{-1} over a 1 cm^3 volume at 690 nm. Indeed, the value of the equivalent $\Delta\mu_a$ depends only on the μ_s' of the homogeneous medium, thus it changes with the laser wavelength (see Table 2 for the precise values).

Table 2. Values of the optical properties (μ_a and μ_s') of the homogeneous phantom and of the absorption perturbation ($\Delta\mu_a$) given by the 100 mm^3 totally absorbing cylinder as a function of the laser wavelength.

Laser Diode number	Wavelength (nm)	Phantom optical properties		$\Delta\mu_a$ over 1 cm^3 (cm^{-1})
		μ_a (cm^{-1})	μ_s' (cm^{-1})	
LD 1	1064	0.21	5.9	0.21
LD 2	1030	0.31	6.13	0.21
LD 3	980	0.55	6.52	0.20
LD 4	940	0.25	6.87	0.20
LD 5	915	0.15	7.1	0.19
LD 6	830	0.11	8.0	0.18
LD 7	670	0.10	10.5	0.16
LD 8	635	0.10	11.2	0.16

The homogeneous phantom was contained into a tank whose front face had a Mylar (50 μm thickness) window, where the optode was placed. To avoid light channelling we spread a thin layer of diffusive US-gel between the Mylar window and the optode surface [5]. After each single cycle of measurements, the perturbation was moved deeper and deeper, from 2.5 mm to 45 mm with respect to the optode surface (distances refer to the perturbation center) by means of a motorized slit with a step precision of 10 μm. For each position of the inclusion, all lasers shone sequentially. For each laser, acquisitions of several values of the gate delay (i.e. different enabling time of the detector with respect to the laser peak time) were made. The gate delays were kept equal for all LDs of the optode. For each acquisition, we recorded photons with an integration time of 15 ms. This integration time has been selected as a trade-off between the need to avoid the saturation of the histogram (as the maximum number of stored events per bin is limited to 4096) and the latency between different acquisitions introduced by the optode communication software (specifically developed by MPD and POLIMI for optode validation purposes) that is about 13 ms. After the signal acquisition, a measurement of the background (without laser) for all delays with the same number of SPADs ON as for the measurement was made to allow precise post-processing background subtraction. The measurement cycle was repeated 67 times and curves summed to get an overall acquisition time of 1 s, as defined by the nEUROPt protocol. For the large source-detector distance (SDD), only one delay ("delay 1") with the whole DTOF (i.e. equivalent to a free-running acquisition) was acquired, while all other gate delays were chosen to select different later portions of the curve, thus enhancing the achievable information in depth [9]. For the short SDD we could not perform a full acquisition in the free-running-equivalent condition with an integration time of 15 ms due to the saturation of the histogram. However, it is well known (as predicted by theory [10]) that short SDD measurements with free-running acquisition are not possible due to strong burst of early photons, which do not carry useful information having investigated only the surface of the scattering medium under investigation. Hence, for the short SDD, the first acquisition ("delay 1") is performed at the earliest delay of the gate window allowing one to avoid such saturation.

To evaluate the depth sensitivity, we made use of 2 figures of merit: contrast (C) and contrast-to-noise ratio (CNR) computed inside a time window (i.e. software selection of a temporal portion of the curve). The former gives information about the visibility of the perturbation while the latter is an indicator of the robustness of the contrast with respect to the noise of the measurement. More in detail, they are defined in the nEUROPt protocol as follows:

$$C = \frac{N_0(t_W) - N(t_W)}{N_0(t_W)}$$

$$CNR = \frac{N_0(t_W) - N(t_W)}{\sigma\left(N_0(t_W)\right)}$$

where N_0 and N are respectively the number of counts within a time window t_W in the homogeneous (i.e., without the perturbation) and heterogeneous (i.e., perturbation inside the phantom) cases, while the $\sigma(N_0(t_W))$ is the standard deviation of the number of counts in the homogeneous case (in the time window t_W) computed over the different measurement cycles. Since the time windows were kept constant for all the lasers, they were chosen in order to optimize the results in the majority of the LDs.

To acquire the homogeneous curve, we moved the perturbation 47 mm in depth, where its effect was negligible. Additionally, the homogeneous measurement was repeated after each movement of the inclusion, to reduce any effect of a possible laser/detector drift in the contrast and CNR calculation.

Before the calculation of the two figures of merits, firstly the counting loss due to the dead-time of the TDC was corrected (following the formula reported in Ref [4]) and then the background subtraction was applied. On the obtained curve, the contrast was computed for each measurement cycle and then averaged.

The measurement was done using both the long and the short SDDs (i.e. shining lasers of optode 2 and 4 respectively).

RESULTS AND DISCUSSION

Figure 8 and Figure 11 report the raw curves acquired using the short and the long SDD respectively. Black and orange rectangles show the time window used to compute contrast for the first (i.e. equivalent to free running) and all others gate delays respectively. The time window width was set to 1400 ps.

Figure 9 and Figure 12 report the contrast obtained for both small and large SDDs. All points with CNR < 1 were removed since the corresponding contrast is not robust. On the other hand, Figure 10 and Figure 13 represent the obtained CNR in the same measurements. Each graph shows the results obtained for a single LD while the different colors encode different gate delays used for acquisition.

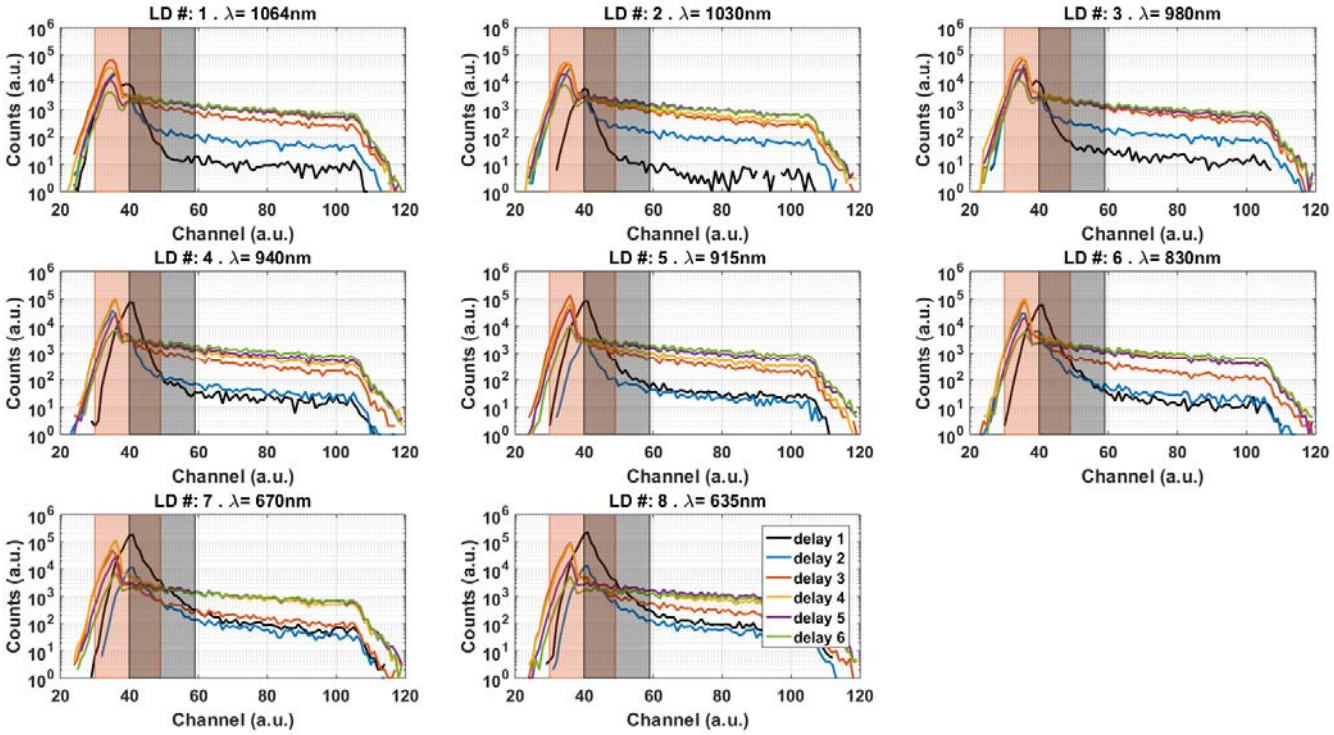

Figure 8. Raw curves acquired for implementation of the NEUROPT protocol at short SDD (using all LDs of optode 4). Grey rectangles show the time window used for the analysis of the "delay 1" curve (i.e. the earliest delay permitting to avoid the saturation of the histogram), while the orange rectangle shows the time window used for all other delays.

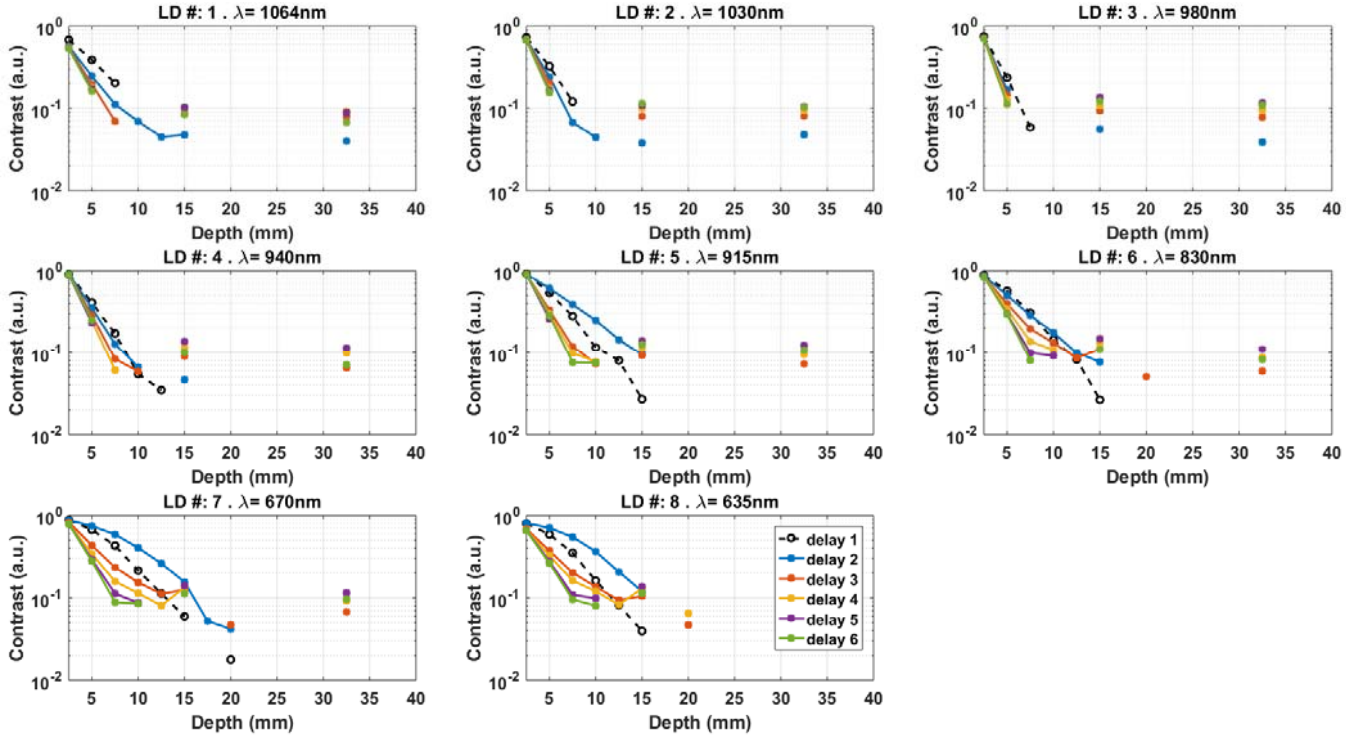

Figure 9. Contrast computed at short SDD for all LDs (different graphs), enabling the detector at different delays (different line colors).

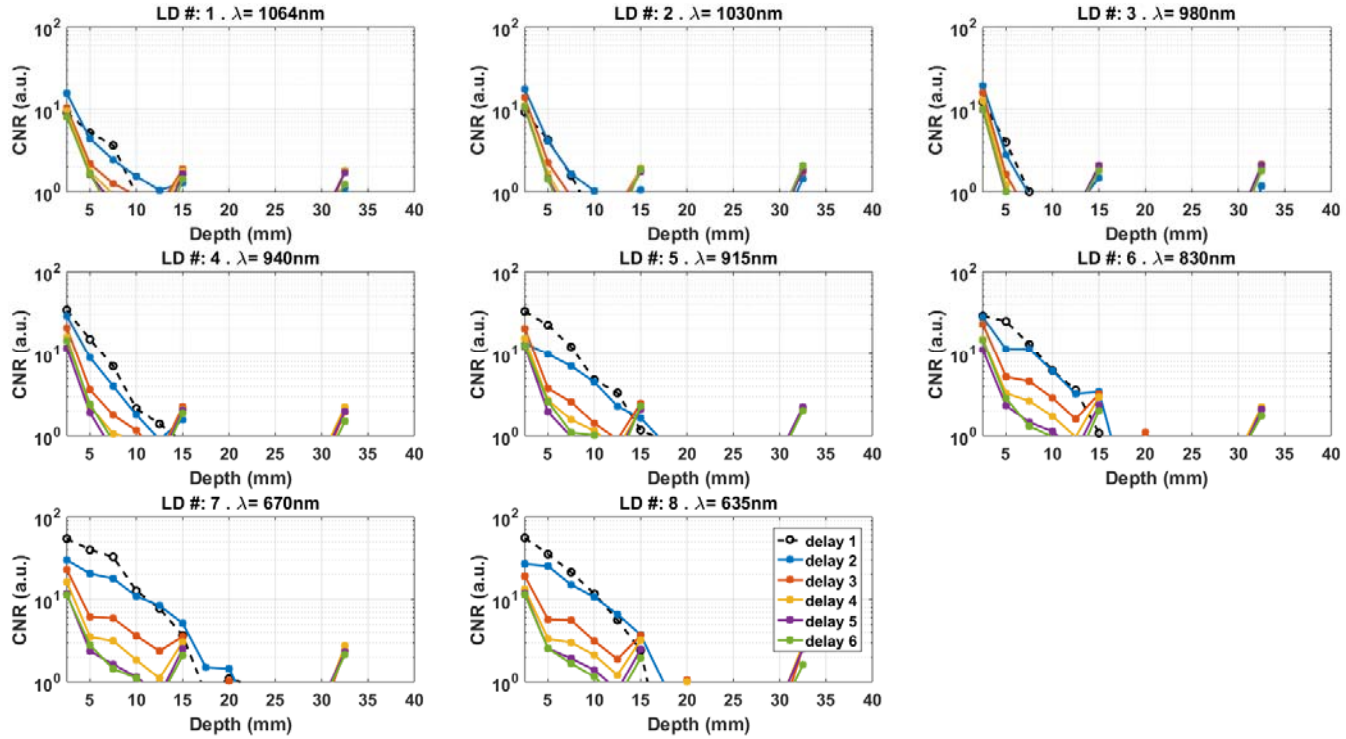

Figure 10. CNR computed at short SDD for all LDs (different graphs), enabling the detector at different delays (different line colors).

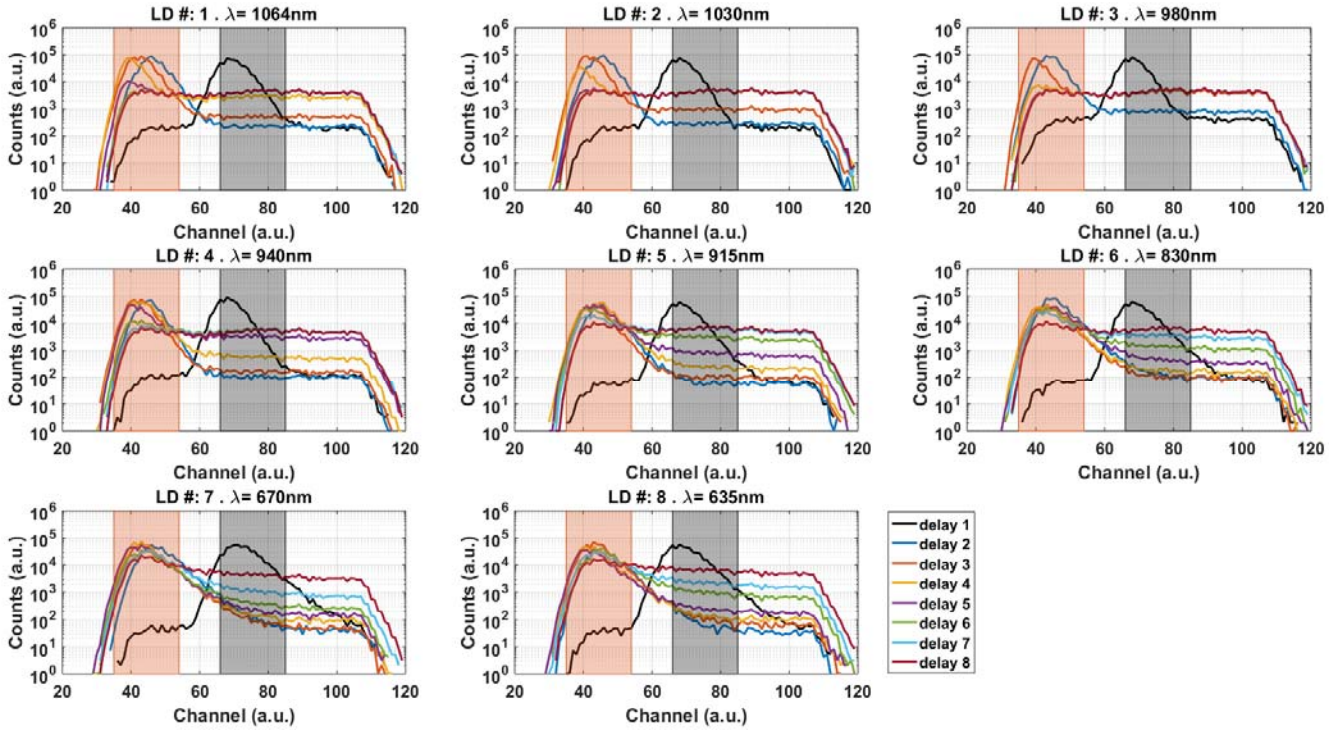

*Figure 11. R*aw curves acquired for implementation of the NEUROPT protocol at long SDD (using all LDs of optode 2). Grey rectangles show the time window used for the analysis of the "delay 1" curve (i.e. equivalent to the free-running acquisition), while the orange rectangle shows the time window used for all other delays.

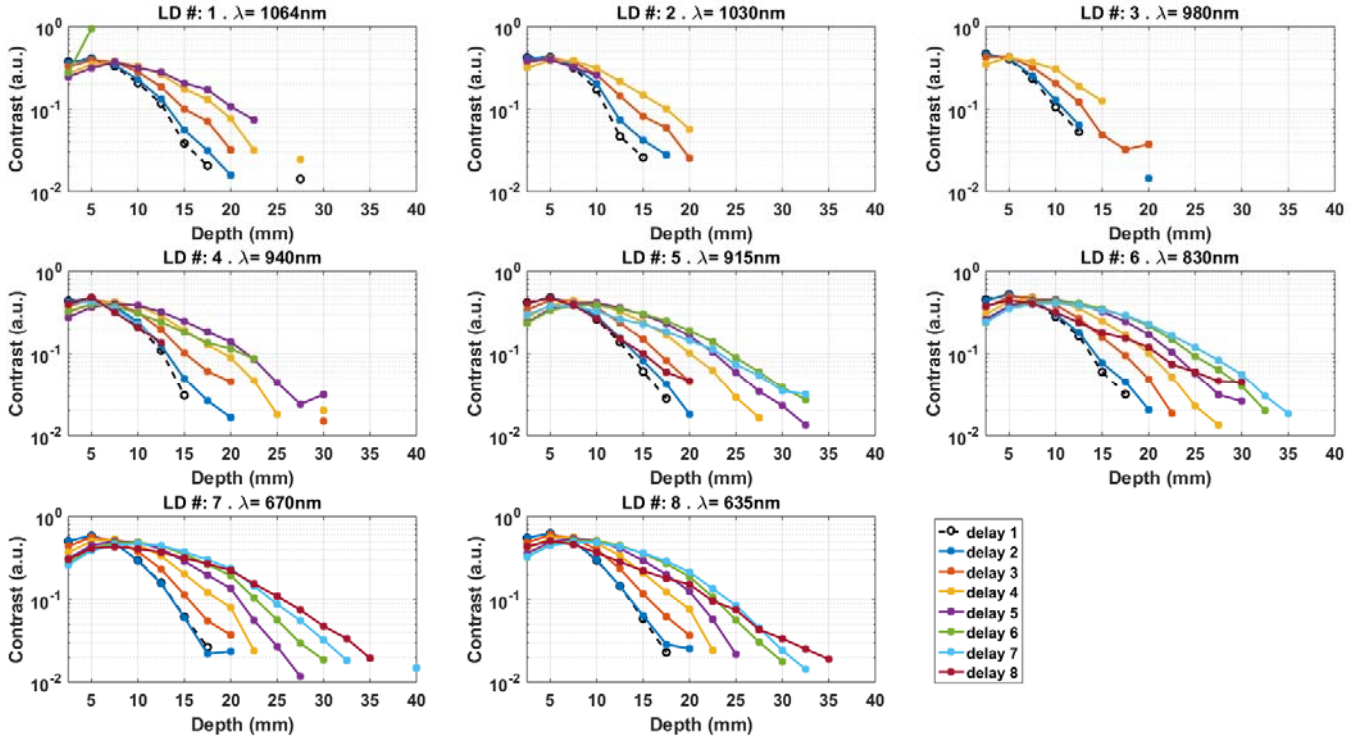

Figure 12. Contrast computed at long SDD for all LDs (different graphs), enabling the detector at different delays (different line colors).

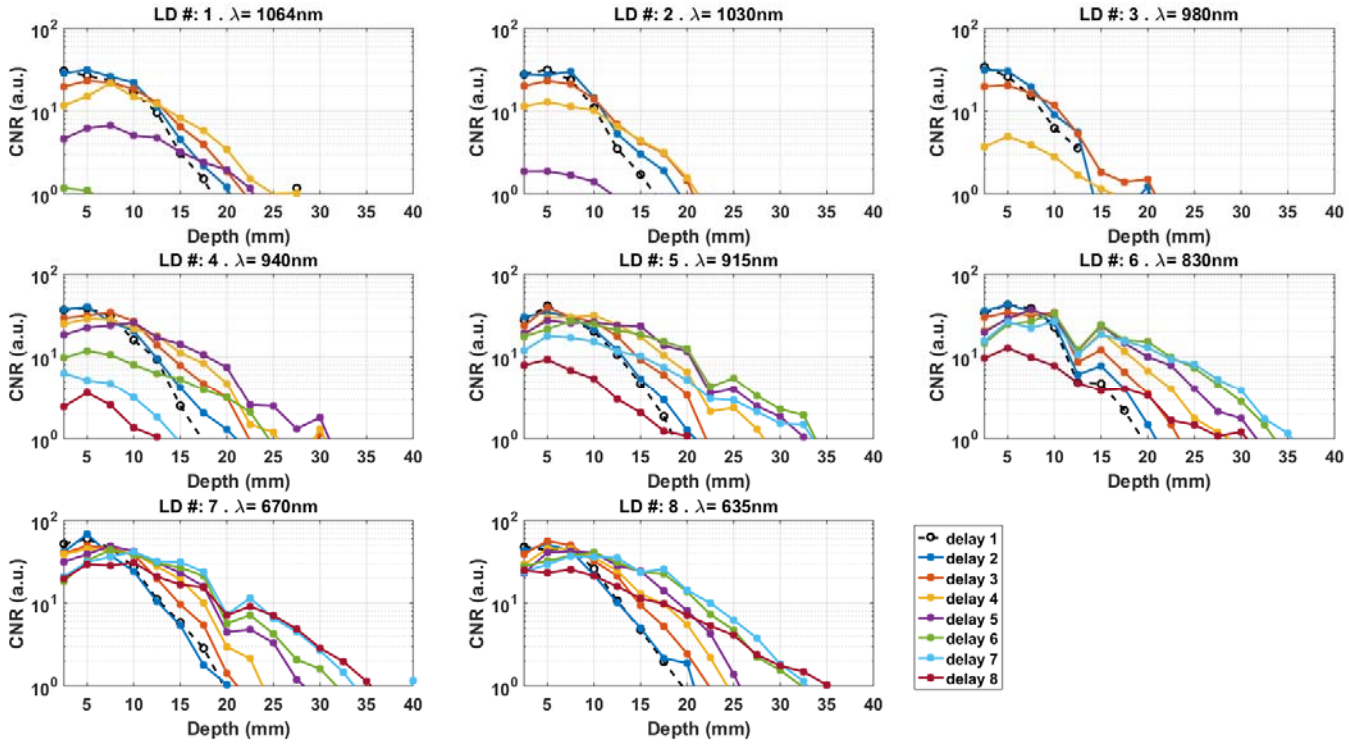

Figure 13. CNR computed at long SDD for all LDs (different graphs), enabling the detector at different delays (different line colors).

Looking at the contrast graphs it is clear that, in agreement with the theory, the penetration depth is highly dependent on the laser wavelength. Indeed, as shown in Table 2, the optical properties of the phantom as well as the optical perturbation drastically change with the wavelength. Moreover, as predicted in [11], measurements with the shorter SDD clearly show a lower penetration depth, most probably due to an additional background floor (the so called "memory effect" [12]) which is proportional to the number of early photons impinging on the detector when it is off.

In light of the previous considerations, to assess the depth sensitivity (KPI 3) we will focus on measurements obtained using the sources of optode 2 and, more specifically, LD 7 which is the closest to the 690 nm, where the phantom features optical properties closer to the standard condition (i.e. μ_a = 0.1 cm^{-1} and μ_s' = 10 cm^{-1}).

Both Figure 9 and Figure 12 clearly show that longer gate delays feature higher contrast for deeper position of the perturbation since the later the photons are re-emitted the higher is the probability they travelled deep in the medium. By focusing on LD7 of optode 2 (see Figure 12), it is clear that the higher penetration depth is obtained using the 8th delay, which allows one to discriminate the presence of a perturbation down to 35 mm with a contrast of 2%. It has to be noticed that, for other LDs, the maximum penetration depth is achieved by using earlier gate delays, because in the later ones there was not enough signal, due to the high absorption featured by the phantom. For what concerns the contrast achieved using the smaller SDD, the penetration depth is limited to 20 mm. In summary, for the longer SDD the KPI was approached but not fully reached, probably due to the memory effect.

Figure 10 and Figure 13 show the trend of the CNR and it is possible to see an improved CNR for shallower positions of the inclusion when the shorter SDD is used. However, the CNR computed for LDs of optode 4 decrease much faster, thus limiting the depth sensitivity. On the other hand, the CNR for measurements acquired with LDs of optode 2 is much higher than 1 (i.e. CNR > 5) down to 25 mm, while it approaches 1 (i.e. the theoretical limit of visibility) for greater depth (up to 35 mm).

4. Capability to retrieve optical properties (MEDPHOT protocol)

INTRODUCTION

The MEDPHOT protocol [3] is meant to assess the capability of diffuse optical instruments like the SOLUS optode to properly retrieve the optical properties of homogeneous scattering media. The MEDPHOT protocol implementation relies on a suitable phantom kit available at POLIMI, which was used in the purpose of this deliverable.

EXPERIMENTAL SETUP AND DATA ANALYSIS

The MEDPHOT phantoms are based on epoxy resin, with the addition of TiO_2 particles and toner, which give the scattering and absorbing properties respectively (for details see Ref. [3]). We made use of 16 phantoms of the MEDPHOT kit divided in 4 series (labeled A, B, C and D), each one characterized by a given reduced scattering coefficient (nominal μ_s' equal to 5, 10, 15, 20 cm^{-1} at 800 nm, respectively). For each series (i.e. given μ_s'), 4 phantoms were measured (those labeled 2, 4, 6 and 8). Each of them has a calibrated quantity of toner to increase the absorption coefficient in nominal steps of about 0.1 cm^{-1} (i.e. nominal μ_a at 800 nm equal to 0.05, 0.15, 0.25 and 0.35 cm^{-1}).

To record the DTOF for each phantom we exploited the fast-gating capability of the detector so as to increase the dynamic range of the measurements [9]. To this extent, for each phantom we acquired the DTOF curve with 17 delays of the detector gating window. For each gate delay an acquisition time of 5 ms (2 ms for phantom of series A to avoid saturation of the histogram) and a proper number of repetitions were made to obtain an overall acquisition time equivalent to 1 s. As for the phantom measurements reported in the previous Section, for each laser diode we recorded the DTOF at all the gate delays and then an equivalent number of background acquisitions (i.e. with all lasers OFF) were carried out keeping the same number of SPADs ON as for the acquisitions with lasers. Before acquiring the data, we waited 15 minutes to warm up lasers and detector. For the present performance assessment, we chose to interpret the data with the most widely applied analytical model, valid in the so-called “diffusion approximation” (i.e. when photons undergo a large number of scattering events). Thus, we performed the measurements at large SDD, using the LDs of optode 2 and the detector of optode 4.

Once the data are acquired, the different repetitions of the measurements were summed up to obtain an equivalent 1 s-curve for each gate delay. Then the correction for the counting loss due to the dead-time of the TDC was performed (following the formula in Ref. [4]), as well as the correction of the DNL and the background subtraction. The curves were then rescaled in time and amplitude. For the former case, they were shifted (i.e. moved to later times) by the value of the gate delay they were acquired with. For the rescaling in amplitude, each curve was divided by a factor proportional to the active area (i.e. number of SPADs ON) used to acquire that gate. The resulting rescaled curves are shown in Figure 14 (DTOFs obtained from B2 phantom). Following the technique described in Ref. [9], after the rescaling of the curves, each DTOF was elaborated to remove the non-linear region just after the opening of the gate and the late part where background noise is dominant, thus extracting a portion of about 350 ps for each gate delay. Since this portion is larger than the step between two consecutive gate delays, the acquired slices are partially overlapping. Each bin of the histogram of the reconstructed DTOF at high DR is thus obtained averaging all the portions overlapping in that bin. An example of cropped curves as well as the final DTOF (black curve) obtained for all LDs with the B2 phantom are reported in Figure 15.

The above described procedure was used to acquire both the IRF and phantom DTOFs. For what concerns the IRF, in this case it was measured putting the optode on a black PVC plane, where a groove was dug and lined with an aluminium foil to allow light propagation from optode 2 (where the LDs are hosted) to the detector in optode 4. The length of this path was measured and the delay due to the propagation of light in this recess was taken into account while fitting the data. For the phantom measurements, we spread a thin layer of diffusive US-gel between the optode and the sample surface to avoid light channelling [5].

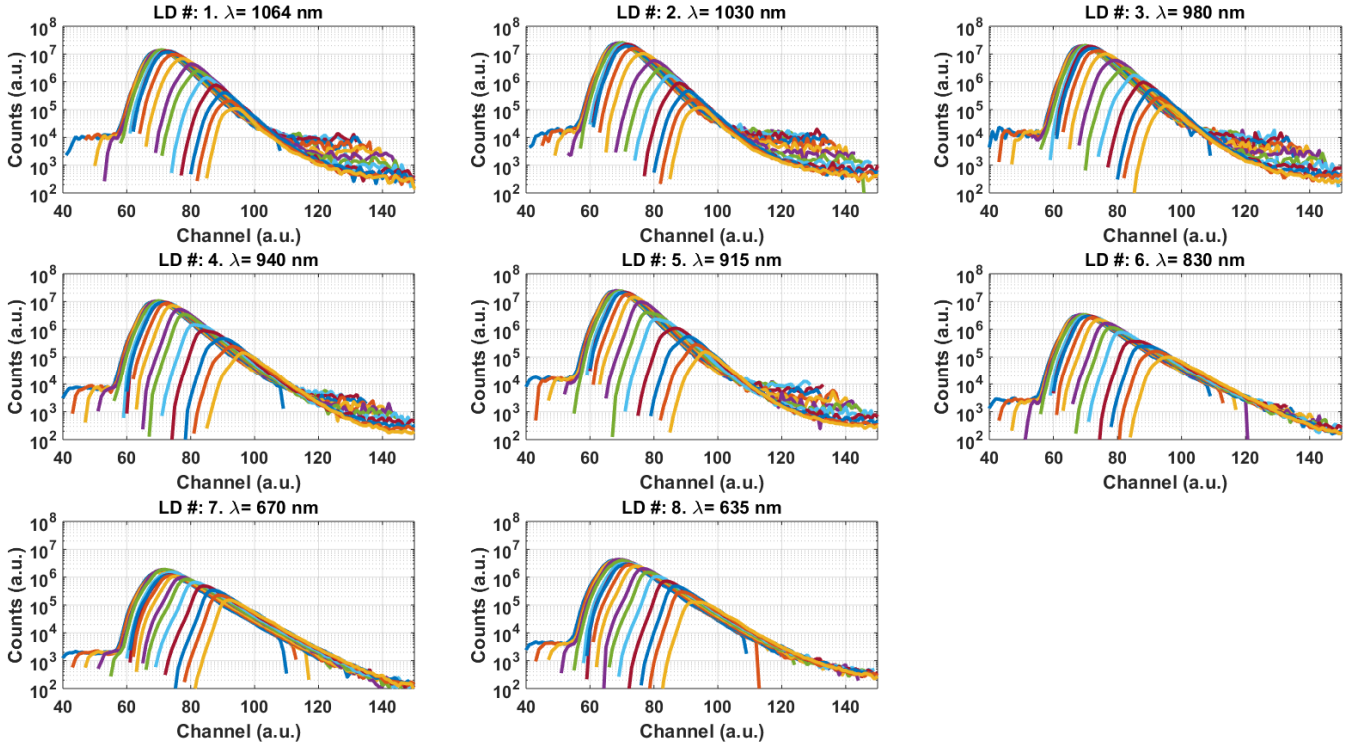

Figure 14. Example of rescaled (both in time and amplitude) DTOFs of the B2 phantom. Different colors show the 17 gate delays acquired for each LD.

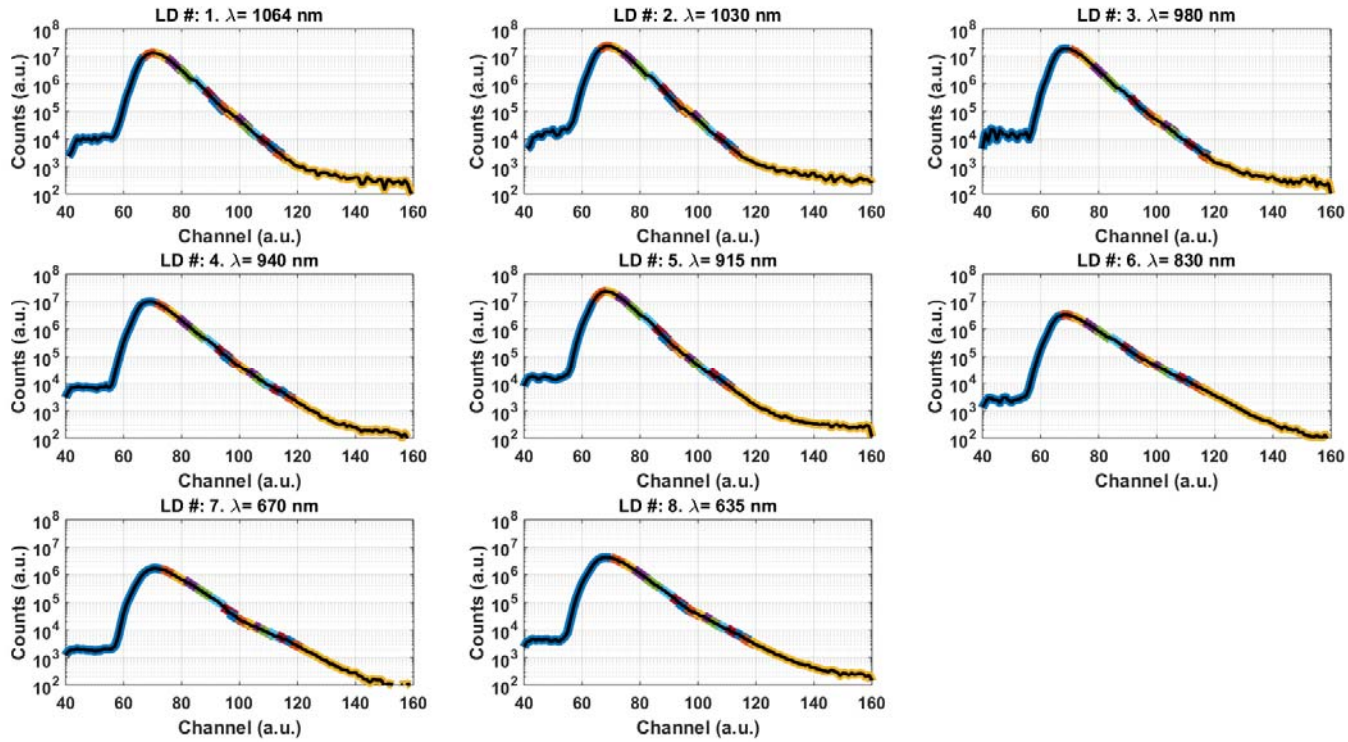

Figure 15. Example of cropped DTOFs of the B2 phantom. The final DTOF (black line) is the average of the cropped contributions given by each of the 17 gate delays (encoded in colors).

For what concerns the optical properties retrieval, we used a fitting algorithm exploiting the analytical solution of the radiative transfer equation under the diffusion approximation for a homogeneous semi-infinite medium [13]. The non-ideal response of the system was taken into account convolving the theoretical solution with the recorded IRF. The fitting algorithm is based on the minimization of the reduced χ^2 using a Levenberg-Marquardt routine (see Ref [14]). Due to the high dynamic range of the measurements, curves were fitted in a region spanning from the rising edge of the DTOF (80% of the peak value) down to the tail (0.01% of the peak value).

RESULTS AND DISCUSSION

ACCURACY

Table 3 reports the relative error (%) of the retrieved μ_a and μ_s' at 635 nm. The error on the absorption is acceptable, with a median discrepancy of 10% and a maximum relative error of 25%. Conversely, the error on the scattering is quite large, with a median discrepancy of 40% and a maximum error in excess of 160%. This problem is further discussed in the LINEARITY Section.

Table 3. Relative error on the estimate of the absorption and reduced scattering coefficients at 635 nm for the 4x4 combinations of phantoms.

		relative error on μ_a				**relative error on μ_s'**			
	nominal μ_s' (cm^{-1})	*4.3*	*8.5*	*12.8*	*17.0*	*4.3*	*8.5*	*12.8*	*17.1*
nominal μ_a (cm^{-1})	**phantom code**	**A**	**B**	**C**	**D**	**A**	**B**	**C**	**D**
0.061	**2**	-4%	-25%	-17%	-17%	-68%	-47%	-35%	-39%
0.177	**4**	-10%	-13%	-10%	-7%	-57%	-42%	-28%	-14%
0.293	**6**	-13%	-4%	-11%	-3%	-59%	-3%	22%	77%
0.409	**8**	-11%	-1%	-10%	-9%	34%	20%	90%	161%

The accuracy for the other wavelengths shows a similar behavior, with acceptable values for the estimate of μ_a and quite large discrepancy for μ_s'. Table 4 reports the median value of the relative error (always taken in modulus) on μ_a and μ_s' at all wavelengths.

Table 4. Median over the 4x4 combinations of phantoms of the modulus of the relative error on μ_a and μ_s' at the 8 wavelengths.

laser (nm)	**635**	**670**	**830**	**915**	**940**	**980**	**1030**	**1065**
median error on μ_a	10%	10%	14%	10%	23%	22%	19%	15%
median error on μ_s'	40%	35%	56%	42%	41%	73%	68%	60%

LINEARITY

The linearity plots at 635 nm are presented in Fig. 16. The 4 panels represent the dependence of the fitted μ_a (top row) and μ_s' (bottom row) on the conventionally true (nominal) value of the phantom μ_a (left column) and μ_s' (right column). Therefore, the upper/left quadrant and lower/right quadrant display the linearity in absorption and reduced scattering coefficient, respectively. In the ideal case, these should all be lines crossing the origin with unit slope. Conversely, the upper/right and lower/left quadrants identify the residual cross-talk of μ_s' against μ_a and μ_a against μ_s', respectively. In the ideal case, these plots should be horizontal lines. With reference to the results for the SOLUS smart optode, the measurements of μ_a is acceptable, displaying a good linearity against the nominal μ_a and no systematic cross-talk caused by μ_s'. Conversely, the measurement of μ_s' is rather poor, with an irregular distribution of retrieved values and – most of all – a strong absorption-to-scattering coupling (i.e. the value of μ_a strongly alters the retrieved μ_s').

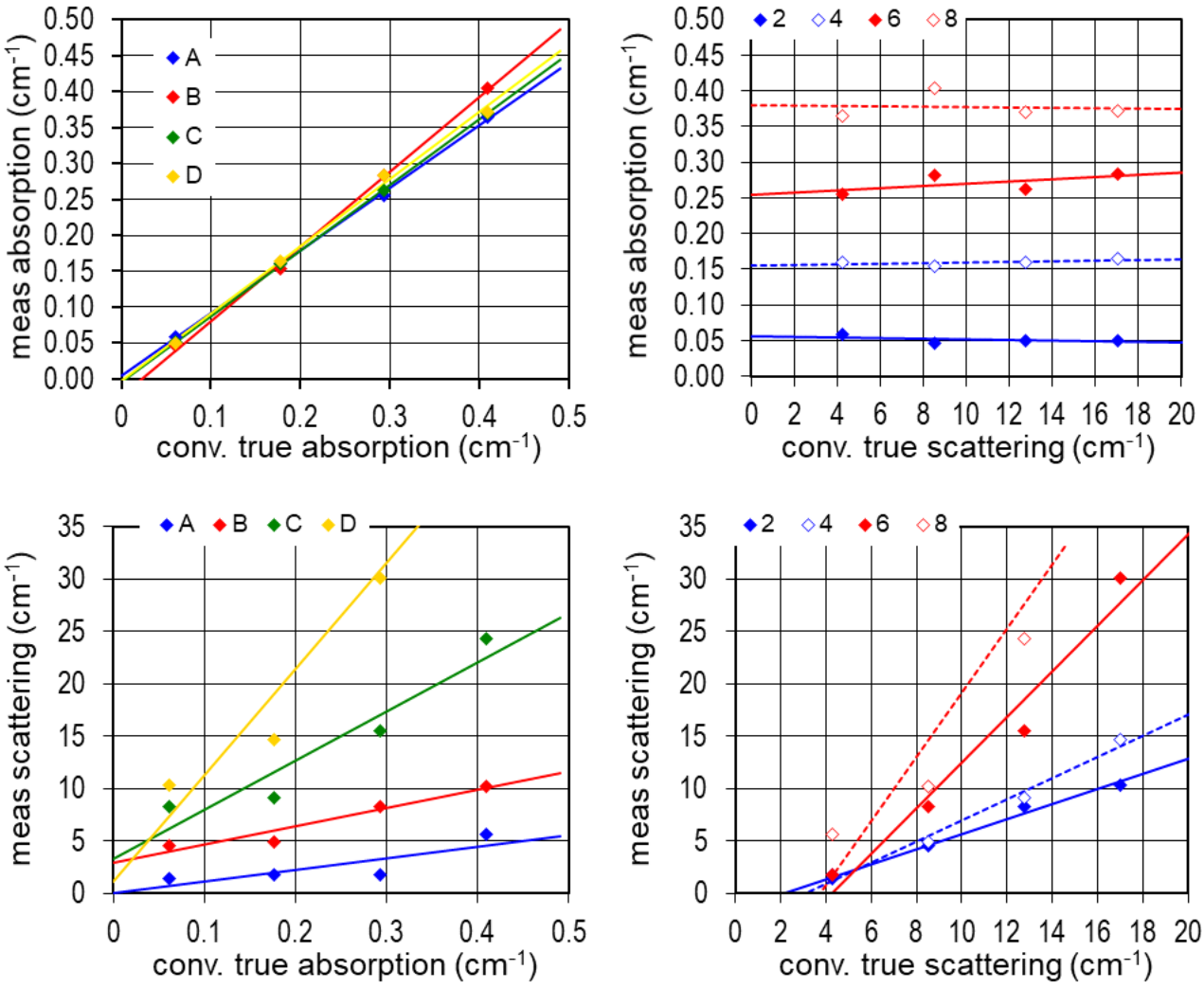

Figure 16. Linearity plots for the retrieved μ_a and μ_s' at 635 nm.

The linearity plots for the other wavelengths show similar trends. The worst performances are obtained at 940 nm, as displayed in Fig. 17. The linearity in μ_a is preserved apart for very low scattering (nominal values ~2 cm^{-1}), which are definitely lower than what expected in clinics for the female breast. As for the scattering, the performances are insufficient mainly due to absorption-to-scattering coupling.

The ultimate reason for this strong coupling is not fully understood yet. The theoretical model is expected to show some limitations at this source-detector distance, yet this should affect mostly the lowest scattering values, which is not the case of interest for tissue measurements. A different reason could be the large collection area of the Optode, which mixes different SDDs in the same measurement. Processing the data using a model of photon migration with a large collecting radius does not cure the problem. More complex approaches – as the tomographic reconstruction – could properly address this issue, but that requires the whole probe to be tested, and goes beyond the scope of the MEDPHOT test. Another reason could be found in the alterations either in the shape of the IRF or in the reconstructed DTOF caused by sub-optimal junctions of the time-gated curves, still the fit of the experimental curve is rather good and it is unlikely this problem will create a systematic effect on μ_s' without altering much the fitted μ_a. A final hypothesis is the presence of stray-light arising from re-emitted photons from the phantom. This aspect is not easy to control and should be studied with the whole probe, where effective light shielding and coupling will be different.

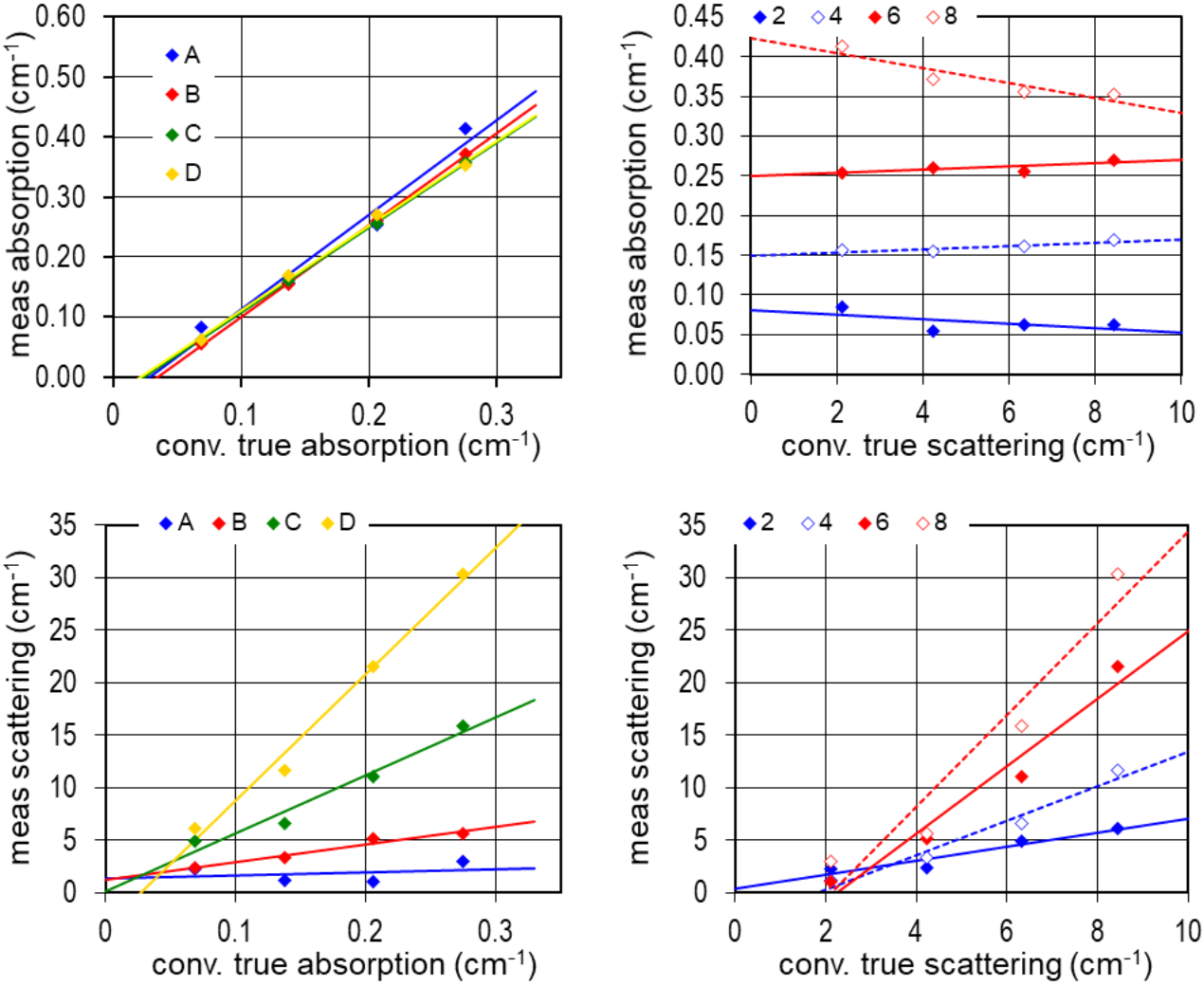

Figure 17. Linearity plots for the retrieved μ_a and μ_s' at 940 nm.

5. Conclusions

On the basis of the tests performed, the following conclusions can be drawn:

- BIP protocol: the optode shows performances in the assessment of the distribution of time-of-flight (shape, signal-to-noise ratio and stability) in line with the state of the art. There are no particular criticalities to highlight.
- NEUROPT protocol: the optode is capable to detect a reference perturbation at a depth of 35 mm adopting the larger source-detector distance. The goal of 40 mm (KPI3) is approached but not reached, possibly due to memory effect.
- MEDPHOT protocol: both accuracy and linearity on the measurement of μ_a is acceptable. Conversely, the estimate of μ_s' is severely affected by a strong absorption-to-scattering coupling.

The overall results are encouraging, considering also the fact that these performances are obtained through an innovative few cm^3 compact fiber-less device. Yet, the maximum reached depth is slightly lower than what foreseen from theoretical predictions and the assessment of μ_s' is severely compromised. For the specific clinical application foreseen – breast cancer discrimination – the key information is conveyed by μ_a (linked to tissue composition) rather than by μ_s' (related to microstructure, for which the Shear Wave Elastography already provides some hint). Considering also the delay of the SOLUS Project with respect to the initially planned timeline, it was decided to proceed to the following phase (probe integration). Still,

research will continue in parallel on the observed criticalities so to try to anticipate and face possible problems in the tomographic reconstruction.

6. References

[1] H. Wabnitz, D.R. Taubert, M. Mazurenka, O. Steinkellner, A. Jelzow, R. Macdonald, D. Milej, P. Sawosz, M. Kacprzak, A. Liebert, R. Cooper, J. Hebden, A. Pifferi, A. Farina, I. Bargigia, D. Contini, M. Caffini, L. Zucchelli, L. Spinelli, R. Cubeddu, and A. Torricelli, "Performance assessment of time-domain optical brain imagers, part 1: basic instrumental performance protocol," J. Biomed. Opt. 19, 86010 (2014).

[2] H. Wabnitz, A. Jelzow, M. Mazurenka, O. Steinkellner, R. Macdonald, D. Milej, N. Zolek, M. Kacprzak, P. Sawosz, R. Maniewski, A. Liebert, S. Magazov, J. Hebden, F. Martelli, P. Di Ninni, G. Zaccanti, A. Torricelli, D. Contini, R. Re, L. Zucchelli, L. Spinelli, R. Cubeddu, and A. Pifferi, "Performance assessment of time-domain optical brain imagers, part 2: nEUROPt protocol," J. Biomed. Opt. 19, 86012 (2014).

[3] A. Pifferi, A. Torricelli, A. Bassi, P. Taroni, R. Cubeddu, H. Wabnitz, D. Grosenick, M. Möller, R. Macdonald, J. Swartling, T. Svensson, S. Andersson-Engels, R. L. P. van Veen, H. J. C. M. Sterenborg, J.-M. Tualle, H. L. Nghiem, S. Avrillier, M. Whelan, and H. Stamm, "Performance assessment of photon migration instruments: the MEDPHOT protocol.," Appl. Opt. 44, 2104–2114 (2005).

[4] W. Becker, The BH TCSPC Handbook 6th Edition (2014).

[5] L. Di Sieno, D. Contini, G. Lo Presti, L. Cortese, T. Mateo, B. Rosinski, E. Venturini, P. Panizza, M. Mora, G. Aranda, M. Squarcia, A. Farina, T. Durduran, P. Taroni, A. Pifferi, and A. Dalla Mora, "Systematic study of the effect of ultrasound gel on the performances of time-domain diffuse optics and diffuse correlation spectroscopy," Biomed. Opt. Express 10, 3899–3915 (2019).

[6] L. Spinelli, M. Botwicz, N. Zolek, M. Kacprzak, D. Milej, P. Sawosz, A. Liebert, U. Weigel, T. Durduran, F. Foschum, A. Kienle, F. Baribeau, S. Leclair, J.-P. Bouchard, I. Noiseux, P. Gallant, O. Mermut, A. Farina, A. Pifferi, A. Torricelli, R. Cubeddu, H.-C. Ho, M. Mazurenka, H. Wabnitz, K. Klauenberg, O. Bodnar, C. Elster, M. Bénazech-Lavoué, Y. Bérubé-Lauzière, F. Lesage, D. Khoptyar, A. A. Subash, S. Andersson-Engels, P. Di Ninni, F. Martelli, and G. Zaccanti, "Determination of reference values for optical properties of liquid phantoms based on Intralipid and India ink," Biomed. Opt. Express 5, 2037–2053 (2014).

[7] F. Martelli, A. Pifferi, D. Contini, L. Spinelli, A. Torricelli, H. Wabnitz, R. Macdonald, A. Sassaroli, and G. Zaccanti, "Phantoms for diffuse optical imaging based on totally absorbing objects, part 1: Basic concepts.," J. Biomed. Opt. 18, 066014 (2013).

[8] F. Martelli, P. Di Ninni, G. Zaccanti, D. Contini, L. Spinelli, A. Torricelli, R. Cubeddu, H. Wabnitz, M. Mazurenka, R. Macdonald, and others, "Phantoms for diffuse optical imaging based on totally absorbing objects, part 2: experimental implementation," J. Biomed. Opt. 19, 76011 (2014).

[9] A. Tosi, A. Dalla Mora, F. Zappa, A. Gulinatti, D. Contini, A. Pifferi, L. Spinelli, A. Torricelli, and R. Cubeddu, "Fast-gated single-photon counting technique widens dynamic range and speeds up acquisition time in time-resolved measurements.," Opt. Express **19**, 10735–46 (2011).

[10] A. Torricelli, A. Pifferi, L. Spinelli, R. Cubeddu, F. Martelli, S. Del Bianco, and G. Zaccanti, "Time-Resolved Reflectance at Null Source-Detector Separation: Improving Contrast and Resolution in Diffuse Optical Imaging," Phys. Rev. Lett. **95**, 078101 (2005).

[11] A. Behera, L. Di Sieno, A. Pifferi, F. Martelli, and A. Dalla Mora, "Instrumental, optical and geometrical parameters affecting time-gated diffuse optical measurements: a systematic study," Biomed. Opt. Express 9, 5524–5542 (2018).

[12] A. Dalla Mora, D. Contini, A. Pifferi, R. Cubeddu, A. Tosi, and F. Zappa, "Afterpulse-like noise limits dynamic range in time-gated applications of thin-junction silicon single-photon avalanche diode," Appl. Phys. Lett. 100, 241111 (2012).

[13] F. Martelli, S. Del Bianco, A. Ismaelli, and G. Zaccanti, Light Propagation through Biological Tissue and Other Diffusive Media: Theory, Solutions, and Software (SPIE, 2009).

[14] W. H. Press, S. A. Teukolsky, W. T. Vetterling, and B. P. Flannery, "Numerical recipes in C," Cambridge Univ. Press **1**, 3 (1988).